μCT scans permeability computation with an unfitted boundary method to improve coarsening accuracy

Lesueur, Martin; Rattez, Hadrien; Colomés, Oriol

DOI
10.1016/j.cageo.2022.105118

Publication date
2022

Document Version
Final published version

Published in
Computers and Geosciences

Computers & Geosciences 166 (2022) 105118

Contents lists available at ScienceDirect

Computers and Geosciences

journal homepage: www.elsevier.com/locate/cageo

Research paper

μCT scans permeability computation with an unfitted boundary method to improve coarsening accuracy

Martin Lesueur [a,c,*], Hadrien Rattez [a,b], Oriol Colomés [c]

[a] Civil and Environmental Engineering, Duke University, Durham, NC 27708-0287, USA
[b] Institute of Mechanics, Materials and Civil Engineering (IMMC), Université Catholique de Louvain, B-1348 Louvain-la-Neuve, Belgium
[c] Faculty of Civil Engineering and Geosciences, Delft University of Technology, Stevinweg 1, 2628 CN, Delft, The Netherlands

ARTICLE INFO

Keywords:
Flow simulations
Finite element method
Permeability upscaling
μCT scan
Unfitted boundary method

ABSTRACT

Flow simulations on porous media, reconstructed from Micro-Computerised Tomography (μCT) scans, is becoming a common tool to compute the permeability of rocks. Still, some conditions need to be met to obtain accurate results. Only if the sample size is equal or larger than the Representative Elementary Volume will the computed effective permeability be representative of the rock at a continuum scale. Moreover, the numerical discretisation of the digital rock needs to be fine enough to reach numerical convergence. In the particular case of using Finite Elements (FE) and cartesian meshes, studies have shown that the meshes should be at least two times finer than the original image resolution in order to reach the simulation's mesh convergence. These two conditions and the increased resolution of μCT-scans to observe finer details of the microstructure, can lead to extremely computationally expensive numerical simulations. In order to reduce this cost, we couple a FE numerical model for Stokes flow in porous media with an unfitted boundary method for cartesian meshes, which allows to improve results precision for coarse meshes. Indeed, this method enables to obtain a definition of the pore–grain interface as precise as for a conformal mesh, without a computationally expensive and complex mesh generation for μCT-scans of rocks. From the benchmark of three different rock samples, we observe a clear improvement of the mesh convergence for the permeability value using the unfitted boundary method on cartesian meshes. An accurate permeability value is obtained for a mesh coarser than the initial image resolution. The method is then applied to a large sample of a high-resolution μCT-scan to showcase its advantage.

1. Introduction

Micro-Computerised Tomography (μCT) was first developed to observe the microstructure of dense materials in a non-destructive way for applications such as medicine and material sciences (Tuan and Hutmacher, 2005; Salvo et al., 2003). It was later applied to rock materials and has shown to be a very valuable tool for rocks characterisation (Mees et al., 2003; Cnudde and Boone, 2013). In particular, this technique is at the core of digital rock physics (Andrä et al., 2013; Arns et al., 2005). In this discipline, properties are measured and computed on μCT scans of rocks such as: porosity (Arns et al., 2005; Blunt et al., 2013); mechanical properties (Arns et al., 2002); chemical properties (Godel, 2013); hydraulic properties (Arns et al., 2005; Blunt et al., 2013). We will focus on the latter in this contribution and compute the permeability based on flow simulations on μCT scans images.

The concept of permeability was first introduced by Darcy (1856) as a quantification of the hydraulic conductivity of soils. This parameter plays a critical role in Darcy's law that is also used in rock mechanics to describe fluid flow at the reservoir scale. Permeability is therefore a key parameter to quantify for energy resources engineering (Bjorlykke, 2010). For this type of application, the property was previously measured using wireline-log analysis, well testing and core flooding experiments on samples collected from drilled wells (Ahmed et al., 1991). However, Darcy's law was proven to be a homogenisation of the Stokes formulation (Whitaker, 1986) for a Representative Element Volume (REV) of rock. The REV of any property is defined as the minimum sample size above which the value of the property assessed has converged to a steady-value. The investigation of the effect of the sample size on the results of simulations for Stokes flow simulations in μCT scans has been carried out for many different rock types (Mostaghimi et al., 2012). The REV of permeability for a rock is usually achieved at the scale of mm^3 (Guibert et al., 2015; Mostaghimi et al., 2012), at which μCT scanning operates, except for the well-known exception of

* Corresponding author.
E-mail address: M.Lesueur@TUDelft.nl (M. Lesueur).

https://doi.org/10.1016/j.cageo.2022.105118
Received 17 June 2021; Received in revised form 28 February 2022; Accepted 12 April 2022
Available online 20 May 2022

carbonate rocks (Mostaghimi et al., 2012; Liu et al., 2014). It becomes therefore interesting to compute the permeability directly on μCT scans of the core sample, for its quality of non-destructive method and added advantages of being able to obtain the full tensor of permeability and multiphase flow properties (Blunt et al., 2013; Dvorkin et al., 2008). Moreover, it enables the computation of hydraulic properties on core materials unsuitable to laboratory testing (Arns et al., 2004).

To compute the permeability on CT scan images, several approaches have been used to simulate the fluid flow including finite difference (Mostaghimi et al., 2012; Manwart et al., 2002) and finite element-based methods (Borujeni et al., 2013; Narváez et al., 2013), vortex and cell centred finite volume method (FVM) (Guibert et al., 2015; Petrasch et al., 2008) and lattice Boltzmann method (LBM) (Manwart et al., 2002; Narváez et al., 2013). The FVM and LBM are the most common approaches for this application (Song et al., 2019). Still, recent developments on the finite element method allow to obtain permeabilities in a good agreement with LBM and FVM (Yang et al., 2019). Moreover, FEM has the advantage to natively allow for a simple coupling with other physical processes like mechanical deformation of the solid matrix. Such deformation can have a major effect on permeability evolution (Ghabezloo et al., 2009). In this context, Arbitrary Lagrangian–Eulerian approaches in finite elements are more commonly used (Lesueur et al., 2017; Bertrand et al., 2017; Donea et al., 1982). Keeping in mind further development of this work towards this direction, we are using the Finite Element method in this paper.

Permeability computations from low-resolution CT-scans do not provide accurate values of permeability as sub-resolution porosity is not captured by the imaging method, but is of primary importance for the flow inside the pores (Soulaine et al., 2016). Fortunately, resolution of CT scans have been constantly improving since the technology was developed, obtaining now images above 1000^2 pixels and with a resolution below a few micrometres (Sarker and Siddiqui, 2009; Soulaine et al., 2016; Wang and Fleischmann, 2018). Higher resolutions for the CT scans are particularly important for porous rocks in order to obtain a better characterisation of the pore–grain interface like the detailing of grains' shape, which influences significantly the value of permeability obtained (Beard and Weyl, 1973; Cox and Budhu, 2008; Torskaya et al., 2013). Note that image processing and segmentation methods also allow to improve on the quality of the microstructure recovered (Iassonov et al., 2009; Wang et al., 2019a). In this contribution, we focus on the CT scan images after such processing of the gryscale data, thus we consider that the images present a mathematically well-defined pore–grain interface. Specifically, we operate in this contribution on CT scans that have gone through a global thresholding segmentation as it remains the most common approach to process the greyscale data. For this method, a global grey threshold value is defined to separate the solid from the pores based on the analysis of the images histograms. This simple way of determining the pore–grain interface is not the most accurate and other methods have been developed to better constrain the position of the interface like locally adaptative thresholding (Burghardt et al., 2007) level set methods (Yan et al., 2008) or marching cubes algorithm (Lorensen and Cline, 1987) and the unfitted boundary method described here for the permeability computation could be also applied directly to segmented images obtained from any of those methods.

The higher resolution of CT scans images comes with the constraint of a higher computational effort to run the flow simulation. Indeed, numerical accuracy is obtained when the result of the FE simulation converges towards a single value with decreasing size of the mesh elements, called mesh convergence. For permeability, the mesh convergence for non-conformal meshes is only obtained with a mesh finer than the image resolution, which leads to simulations with a very large number of elements in the case of high-resolutions CT scans. For example, the study of Guibert et al. (2015) showed that a cartesian mesh size of even twice the resolution of the original image could not be enough to reach mesh convergence for permeability. In the case of carbonate rocks, it becomes then extremely difficult to get good accuracy on the value of permeability as the REV size can be very large. In some instances the size needed for the computation is above the capability of the simulator (Guibert et al., 2015) and final permeability value is only computed at the limit of resources. The issue with computational cost in Digital Rock Physics has been reported many times in the literature (Soulaine et al., 2016; Guibert et al., 2015; Torskaya et al., 2013; Wang et al., 2019b; Shah et al., 2016).

While many solutions are developed with the objective to increase the number of elements in a simulation at a lower computational cost (Wang et al., 2019b), we opt for a different approach which aims at reducing the number of elements needed to reach mesh convergence. Such numerical coarsening procedure has already been shown to preserve pore-space properties (Shah et al., 2016). Still, the magnitude of the approximation on permeability due to a too low resolution image can be non-negligible (Guibert et al., 2015; Zakirov and Galeev, 2019; Borujeni et al., 2013). To this end, we are looking for a better approximation of the pore–grain interface for a mesh coarser than the CT scan image resolution. Here we apply an unfitted Finite Element Method (FEM) approach for this numerical coarsening scheme in which the geometry of the domain is embedded in a background mesh. Different methods can be considered for this aim, typically classified in two main groups: immersed boundary methods or embedded boundary methods. The former basically consists on solving the problem in the active and inactive parts of the domain, enforcing the boundary condition via a forcing function (see Mittal and Iaccarino, 2005). In the later approach, the equations are solved only on the active part of the domain and the boundary conditions are enforced by either modifying the weak form of the problem or manipulating the mesh close to the boundary (see e.g. Burman et al., 2015; Rangarajan and Lew, 2014). In this work we propose an embedded boundary method for cartesian meshes in which the nodes of the background mesh at the interface between active and inactive elements are displaced in such a way that they fit the embedded geometry obtained from CT scans with a finer resolution than the mesh considered, see Section 2.1. Note that one of the main differences with respect to the universal meshes approach presented in Rangarajan and Lew (2014) is precisely the use of cartesian grids. By using the latter, we can take advantage of octree-based adaptive mesh refinement strategies (see e.g. Lesueur et al., 2017). Other advantages of this choice are, for instance, the ability to use spectral approximations or highly efficient data-structures.

After a first section on the description of this new method, referred as the displaced boundary method, it is benchmarked for μCT scans of three types of rocks presenting different microstructure geometries. We finally showcase the method's performance for a high-resolution CT scanned rock sample.

2. Displaced boundary method

2.1. Description and numerical implementation

The mesh of the digital rock is constructed using the approach introduced by Lesueur et al. (2017). It relies on the image reader capability of the finite element framework MOOSE (Permann et al., 2020) and produces 3D cartesian meshes of the pore space of rock microstructures reconstructed from a stack of segmented μCT scan images. Our focus is to obtain accurate values of permeability by homogenisation at a reduced computational cost by running simulations on a mesh coarser than the image resolution. In this case, the pore–grain boundary has to be grossly approximated in a given way. Specifically in this contribution, it is the pixel value of the element's centroid that dictates whether the element should be a pore or a grain. This meshing procedure is showcased for the example of a quarter circle in Fig. 1a and the resulting approximation of the boundary can be observed in Fig. 1b.

To use the displaced boundary method introduced here, we need to mesh the digital rock at its full resolution and extract the pore–grain boundary as a STL file. This file contains the geometry of the

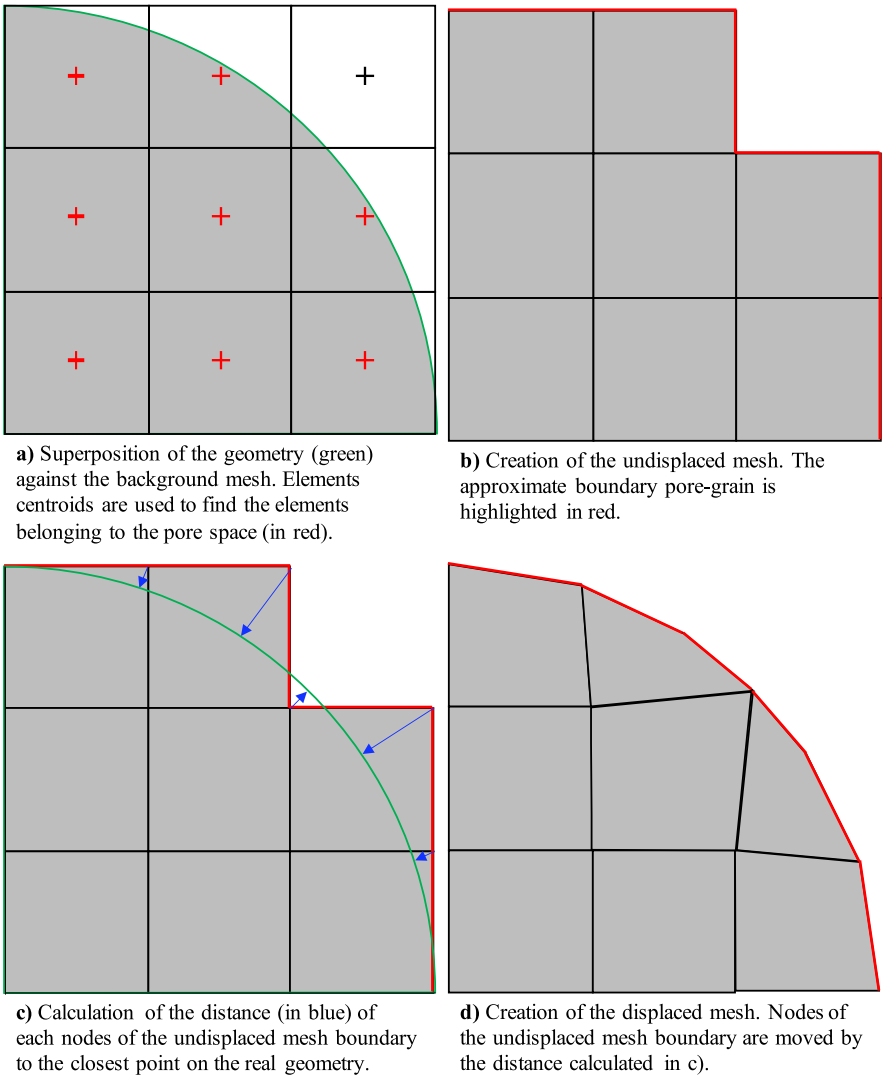

a) Superposition of the geometry (green) against the background mesh. Elements centroids are used to find the elements belonging to the pore space (in red).

b) Creation of the undisplaced mesh. The approximate boundary pore-grain is highlighted in red.

c) Calculation of the distance (in blue) of each nodes of the undisplaced mesh boundary to the closest point on the real geometry.

d) Creation of the displaced mesh. Nodes of the undisplaced mesh boundary are moved by the distance calculated in c).

Fig. 1. Schematic of the meshing procedure of a quarter circle against a 3 × 3 grid using the displaced boundary method. The displaced mesh (d) results in a better approximation of the real geometry than the undisplaced mesh (b). (For interpretation of the references to colour in this figure legend, the reader is referred to the web version of this article.)

pore–grain interface as a surface in three dimensions that we are trying to match with the lower resolution mesh. As a preprocessing step, the distance between the precise interface given by the STL file and the approximated one of the mesh is computed. For each node of the meshed pore–grain boundary, we find the closest point on the STL and return the distance between the two. The distance is displayed for the example of a quarter circle in Fig. 1c. The nodes (and subsequently the integration points) of the mesh are then *displaced* of the computed distance and the pore–grain interface now matches the geometry of image at full resolution. The final result is a mesh with a lower resolution than the image that still matches closely the pore–grain boundary, as can be observed in the example of a quarter circle in Fig. 1d.

Note that this technique can be understood as a process to transform the original background mesh to a conforming mesh. Certain mesh generators can obtain similar conforming meshes such as SnappyHexMesh from OpenFOAM. However, our method is not constrained by the complexity of generating a sophisticated physical mesh. Instead, it is better described as an unfitted FEM approach in which the mesh is fixed and an additional transformation map is applied to the Finite Element reference map. Indeed, this map ($\varphi_{\mathbf{d}}$) can be defined for each background mesh node i, with original coordinates $\mathbf{x}_i$, as

$$\hat{\mathbf{x}}_i = \varphi_{\mathbf{d}}(\mathbf{x}_i) = \begin{cases} \mathbf{x}_i + \mathbf{d}(\mathbf{x}_i) & \text{if } \mathbf{x}_i \in \Gamma_M, \\ \mathbf{x}_i & \text{otherwise.} \end{cases} \tag{1}$$

Where Γ_M is the interface of the background mesh and $\mathbf{d}(\mathbf{x}_i) := \mathbf{x}_{S,i} - \mathbf{x}_i$ the distance from a node i on Γ_M, with $\mathbf{x}_i \in \Gamma_M$, to the closest point on the pore–grain interface Γ_S, $\mathbf{x}_{S,i} \in \Gamma_S$. The closest point on the pore–grain interface is such that it minimises the Euclidean distance $\|\mathbf{x}_S - \mathbf{x}_i\|$ for any point $\mathbf{x}_S \in \Gamma_S$. In this contribution, the "displaced mesh" refers to the equivalent mesh on which the FE simulations are computed. The "undisplaced" mesh corresponds then to the regular cartesian mesh.

The well-posedness of the method is guaranteed if the resulting map leads to transformed elements with a positive Jacobian. In that case, the method inherits all the convergence and stability properties of an standard conformal Finite Element approach. However, this condition is not satisfied in the general case. Nonetheless, in practice,the method of selecting the elements domain (pore or grain) based on the element's centroid (see Fig. 1a) results in an approximated pore–grain interface with a distance to the real interface of, at worst, one element's size h. Therefore, in practice, no negative Jacobians should be found, which was observed in every simulation of this contribution. Further analysis is required to prove theoretical well-posedness. Another drawback of some unfitted FEM approaches is the so called *small cut-cell problem*, which results in ill-conditioned matrices caused by the appearance of active elements with a measure orders of magnitude smaller than the measure of the neighbouring elements. In the approach presented in this work this issue is avoided by only activating the elements whose

centroid lies inside the domain. Therefore, assuming a sufficiently smooth boundary, the measure of the displaced elements is of the same order as the one of the elements from the original background mesh.

The relevance of the proposed approach lies in its efficiency and simplicity of implementation. Comparable results can be obtained with other embedded Finite Element techniques such as in Burman et al. (2015), where a stabilisation term is added to avoid the *small cut-cell problem*. The proposed approach avoids the use of this term and the integration on cut cells, which simplifies the algorithmic simplicity and reduces computational cost associated to the numerical integration.

It is important to highlight that the proposed method does not depend on the way the geometry is characterised. That means that it can be used for geometries defined by STL files generated from CT scanned samples, but also for domains defined by continuous distance fields, e.g the level-set method, or domains defined using CAD techniques. Furthermore, the proposed approach is suitable for non water-tied geometries, i.e geometries defined by non-contiguous parts, as long as a distance field can be provided at the pore–grain interface nodes. In addition, we also note that the proposed approach can be directly applied to adaptively refined or coarsened meshes, as long as the underlying background cells close to the interface are composed by regular squares or hexahedra.

Any computation during the simulation is done on the displaced mesh. The FEM simulator used in this contribution is MOOSE, in which we can do computations on the displaced mesh. The permeability computation is done following the methodology presented in Lesueur et al. (2017), summarised briefly below. Pressure driven stokes flow, expressed in dimensionless form as:

$$-\frac{1}{Re}\nabla^2\vec{v}_{\vec{f}}^{\,*}+\nabla p_f^* = 0 \tag{2}$$

$$-\nabla\cdot\vec{v}_{\vec{f}}^{\,*} = 0 \tag{3}$$

with v_f the fluid velocity, p_f the fluid pressure and Re the Reynolds number. The system of equations is solved using a Pressure-Stabilised Petrov–Galerkin formulation (Hughes et al., 1986). This approach results in a stable weak form for equal order velocity–pressure pairs that is given as: find $(v_h, p_h) \in \mathcal{V}_h \times \mathcal{Q}_h$ such that

$$\int_\Omega \left[\frac{1}{Re}\nabla v_h \nabla w_h - p_h(\nabla\cdot w_h) + q_h(\nabla\cdot v_h) + \tau\nabla p_h\cdot\nabla q_h\right] d\Omega = 0$$

$$\forall (w_h, q_h) \in \mathcal{V}_h \times \mathcal{Q}_h, \tag{4}$$

with $\tau = Reh^2/12$ and h the characteristic element size. The Finite Element spaces, $\mathcal{V}_h$ and $\mathcal{Q}_h$, are defined as: $\mathcal{V}_h = [\mathcal{X}_h]^d$ and $\mathcal{Q}_h = \mathcal{X}_h$, with

$$\mathcal{X}_h = \left\{v_h \in H^1(\Omega) : v_h|_K \in Q_r^d(K),\ v_h|_{K\cap\Gamma} = 0,\ \forall K \in \mathcal{T}_h\right\}.$$

Where Q_r^d is the tensor product in d dimensions of polynomials of order r, and $\mathcal{T}_h$ is the set of active regular quadrilateral or hexahedral elements in the domain Ω. In this work we use linear polynomials, i.e. $r = 1$, resulting in an optimal convergence rate of second-order, $\mathcal{O}(h^2)$. This formulation has been widely used in the literature (Peterson et al., 2018; Codina and Blasco, 2000; Tezduyar and Sathe, 2003) and can be framed within the context of variational multiscale methods (Hughes et al., 1998; Codina et al., 2018; Colomés et al., 2015). Note that the choice of formulation (4) is motivated by the ability to use equal order interpolation elements for velocity and pressure, satisfying the inf-sup condition. However, the method proposed in this work is independent of the stabilisation approach and would directly apply for non-stabilised formulations that use inf-sup stable velocity–pressure pairs, e.g. the Taylor–Hood element. Taking advantage of the solvers of PETSc included in MOOSE, the Schur method is used to precondition the system following Elman et al. (2008). We follow a prescribed solution from Balay et al. (2016) and use a Jacobi preconditioner for the fluid pressure subsystem and the algebraic multigrid method BoomerAMG (Henson and Yang, 2002) from HYPRE for the fluid velocity subsystem. Note that the preconditioning of our system enables to invert rigidity matrix even for elements for not well conditioned elements like in Fig. 1. We would like to note that the proposed method does not affect the algebraic structure of the original problem, allowing the use of scalable solvers for the Stokes problem already available in MOOSE (Peterson et al., 2018; Permann et al., 2020).

2.2. Permeability computation

From the computed flow, the average velocity in the selected direction is post processed on the displaced mesh. The permeability is finally calculated using the formula:

$$k = \mu_f\ L_{ref}\frac{\phi\ v_f^*}{\Delta p_f^*} \tag{5}$$

with μ_f the fluid viscosity, ϕ the porosity and L_{ref} the reference length. The influence of the method on the value of permeability is showcased conceptually in Fig. 2. A perfect semi sphere is meshed at a lower resolution in Fig. 2a, with 10 elements for the diameter. We use the displaced method to retrieve the smooth geometry of semi-sphere in Fig. 2b. The difference of geometry between the two meshes is reflected in the computed permeability through the porosity first, used in Eq. (5). In addition, this geometrical difference affects in turn the fluid flow. Instead of the fluid flowing through the virtual corners created by the boundary approximations in Fig. 2a, we observe the expected smooth flow around the displaced mesh of the sphere in Fig. 2b. This is the second influence on the permeability, specifically on the average velocity computed, which is used in the permeability formula, Eq. (5).

2.3. Sphere packing benchmark

We demonstrate the advantage of the method on a benchmark of the semi-analytical solution for the permeability k of a Simple Cubic Packing of spheres of diameter d_{sp}. Sphere packings represent the ideal benchmark for the computation of permeability on CT scans. Whilst remaining simple enough for semi-analytical solutions to exist (Zick and Homsy, 1982; Sangani and Acrivos, 1982; Larson and Higdon, 1989), they are representative enough of granular media and reproduce the challenges of computing flow through granular media. Additionally they represent a simple example of the geometrical challenge tackled in this study which is the presence of curved interfaces discretised with a cartesian mesh.

We follow the setup of Zick and Homsy (1982) and select a concentration of spheres of 0.45 (corresponding to $d_{sp} = 0.95076$) assembled as a non-overlapping Simple Cubic Packing. The modelling of the packing's behaviour is reduced to the study of one unit cell by using periodic boundary conditions. Furthermore, based on the symmetry of the problem, only a quarter of sphere is meshed (oriented in the flow direction) and slip boundary conditions are imposed on the sides for the solution to be representative of the full unit cell. The set-up of the benchmark is schematised in Fig. 3b. A mesh convergence of the permeability is computed on both the regular hexagonal mesh and the displaced mesh and we plot in Fig. 3 the error with regards to the semi-analytical solution of Zick and Homsy (1982) for both methods. Note that the drag force F_d, reported in Zick and Homsy (1982) is converted to a permeability value using the formula of Gerke et al. (2018),

$$F_d = \frac{d_{sp}^2}{18(1-\phi)k}. \tag{6}$$

We can see that the displaced method, in red, is already below 1% of error with only 40 elements for the unit cell length, whereas the regular hexagonal mesh leads to an error of still a few percent of error even at 150 elements. We can also observe in Fig. 3 the different orders of convergence (the slope of curves) between the undisplaced and displaced methods, linear and quadratic respectively. Note that in the undisplaced case, since we do not capture properly the boundary,

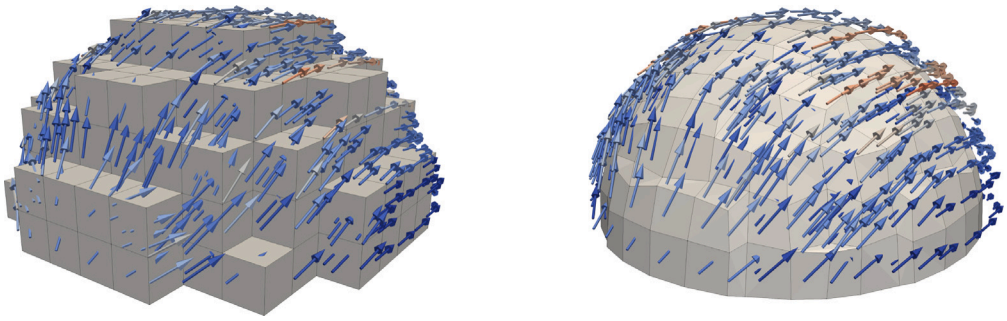

Fig. 2. Oriented fluid flow vectors coloured with relative magnitude around a demi sphere, traditionally meshed (a) and displaced (b). The sphere is meshed with 10 elements in diameter for both figures. (For interpretation of the references to colour in this figure legend, the reader is referred to the web version of this article.)

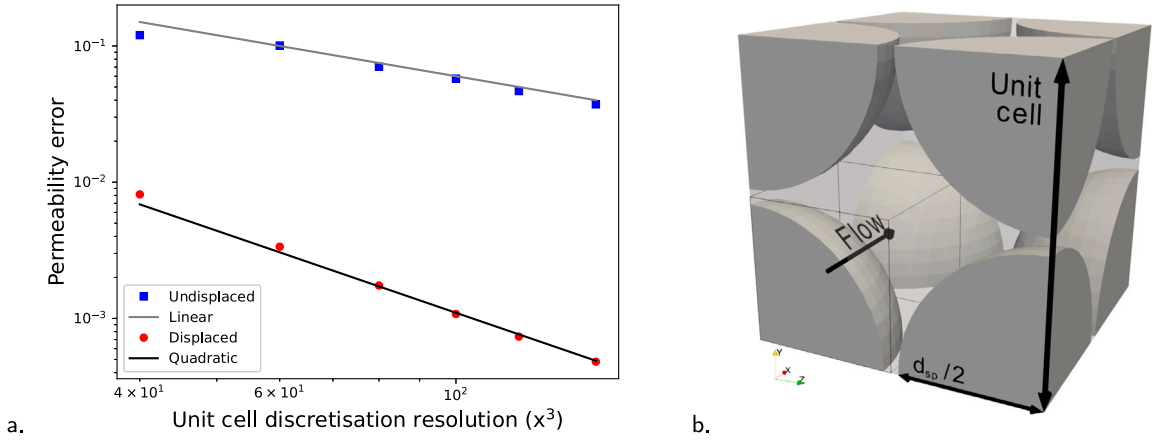

Fig. 3. Permeability error compared to the semi-analytical value of Zick and Homsy (1982) for a Simple Cubic Packing of spheres of concentration 0.45 ($d_{sp} = 0.95076$ of the unit cell), using both the undisplaced and displaced boundary method (left). The set-up of the simulation is displayed on the right. The unit cell is taken as the pore space located in between the spheres, highlighted in transparent grey. Thanks to the symmetry of the system, the simulation can be made on only a quarter of the unit cell, shown with the wireframe box. Quadratic convergence of the error can be appreciated with the displaced boundary method (fitted with $11x^{-2}$ in black) while the undisplaced method has only a linear convergence (fitted with $6x^{-1}$ in grey).

the solution will be subject to an error at least of the order of the element size. Therefore, since we use stabilised linear Finite Elements with optimal quadratic convergence rate, see for instance Burman and Fernández (2011), the convergence rate of the solution will be at most linear. On the contrary, the proposed displaced approach results in a conformal discretisation of the boundary, leading to the expected optimal convergence rate (quadratic). Such a smooth convergence allows to be more predictive on the extrapolation of the converged value.

Fig. 4a shows the added percentage of computation time needed when using the displaced boundary method, for this numerical study. Compared to the standard approach, the additional operations in the proposed method is the computation of distances to the interface and the initialisation of the displaced mesh. For the set-up of Fig. 4, the interface of the STL file has a resolution 2^3 times higher than the largest simulation, consistent with the range of relative resolutions studied in this contribution. We can observe that for small simulations, the displaced boundary method adds a consequent amount of computation time, explained by the fact that the distance is computed for an image that has a relatively much higher resolution that the mesh. When considering however a higher mesh resolution, the limiting process becomes the initialisation of the displaced mesh that converges towards adding ≈15% computation time. For this range of application, the distance computation operation adds a relatively negligible amount of time thanks to the efficiency of the close point projection methods (we rely on the libigl library (Jacobson et al., 2018) in this contribution). Despite the added time of the displaced boundary method, it is still profitable to use it as we see in Fig. 4b that the error, even scaled with computation time, remains lower than the one obtained with the regular cartesian mesh.

3. Method performance

In order to showcase the method's performance on rock permeability computation, we compare the mesh convergence with and without the displaced boundary method for three completely different rock samples. We select the LV60 A sandpack (Imperial College Consortium On Pore-Scale Modelling, 2014a), the S1 sandstone (Imperial College Consortium On Pore-Scale Modelling, 2014b) and finally, the Ketton limestone. Note that the samples are not necessarily REV since the focus of this study is only to assess the permeability computation accuracy of our method for a given image. As observed in Fig. 5, the nature of the rock studied changes its microstructure. In addition, the CT scanning process influences the digitisation of said microstructure. The differences that can be observed between the samples given the CT scanning resolution are listed below:

- **Granularity** The sandpack and the limestone are granular. It is harder to distinguish the grains in the sandstone as they are heavily cemented to each other. The rock matrix forms instead an interconnected skeleton.
- **Roundness** The sandpack and sandstone have grains that can be of various shapes, elongated or compact. The limestone instead have very round grains.
- **Grain size** The sandpack is known for having a very homogeneous grain size distribution. It differs from the limestone where a big contrast of size exists between some grains.
- **Spatial resolution** The limestone has been CT scanned at a much higher resolution with regards to its grain size than the other two rocks which results in a well-defined pore–grain interface.

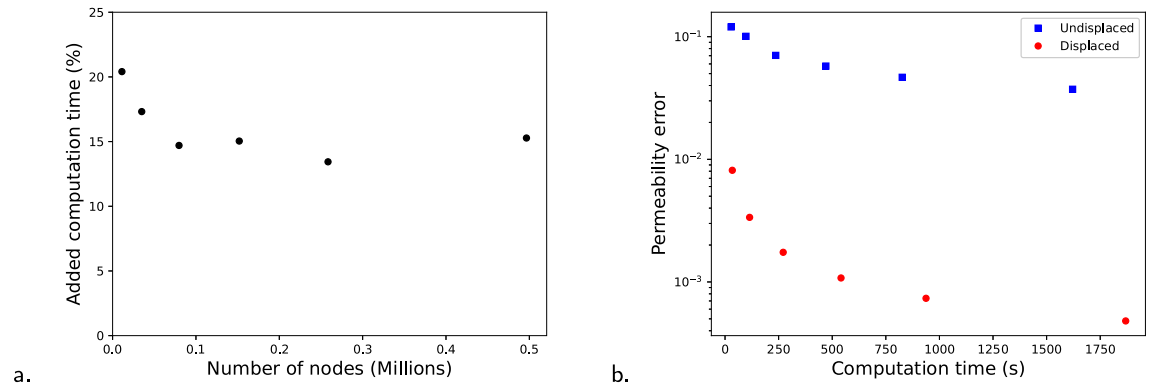

Fig. 4. Evolution with mesh size of the computation time taken by the displaced boundary method in the numerical study presented in Section 2.3 relatively to the total computation time of the regular simulations (left). Scaling of the permeability error with total computation time for both methods (right). The simulations were run in serial with the solver presented in Section 2.1.

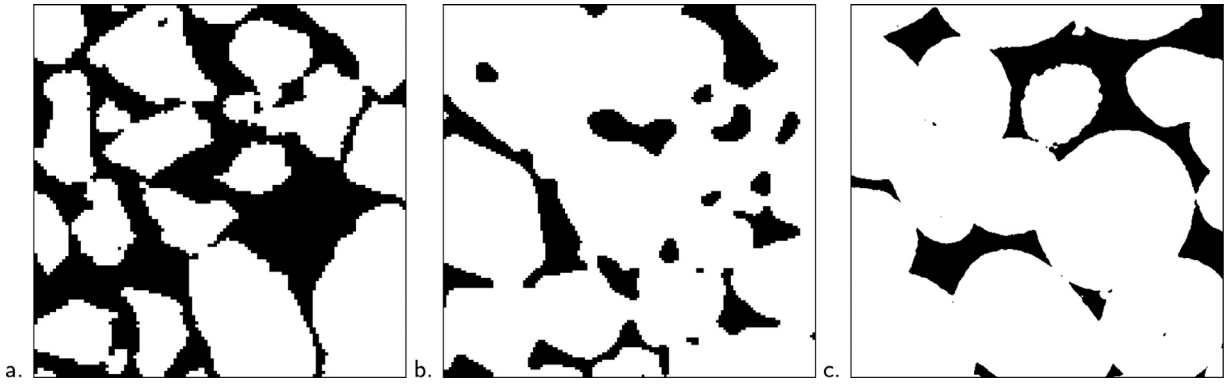

Fig. 5. Visualisation of grains (white) and pore space (black) on a segmented slice of the samples studied. (a) The LV60 A sandpack (Imperial College Consortium On Pore-Scale Modelling, 2014a) with a spatial resolution of 10.002 μm (sample size of (1.2 mm)^2). (b) The S1 sandstone (Imperial College Consortium On Pore-Scale Modelling, 2014b) with a spatial resolution of 8.683 μm (sample size of (1.3 mm)^2). (c) The Ketton limestone with a spatial resolution of 3.00006 μm (sample size of (1.5 mm)^2).

On the other hand, we can almost visualise the pixels in Fig. 5a, which results in a staircase type pore–grain interface. The exact resolutions are listed in the caption of Fig. 5.

By selecting such a diverse array of samples, we aim at emphasising on the generic nature of the method, that can be applied to any rock's CT scan.

The permeability is computed on 3D subsets of the samples of Fig. 5 using the flow simulator and permeability postprocessing of Section 2.1. For each sample, the mesh convergence of permeability is established with and without the displaced boundary method and the results are plotted in Figs. 6, 7, 8. We note that our method has no impact at the CT scan original resolution (denoted by a green vertical line) because the distance computed would then be zero. However, a difference in resolution of one element is sufficient to fall back on the mesh convergence curve of the displaced method, which we applied for the curves of this contribution. The phenomenon is also present at half of the resolution of the CT scan but is less impactful.

In order to better observe the mesh convergence, the numerical error on permeability is plotted in addition to the absolute value of permeability. Since the reference value is not known for the samples considered, unlike Fig. 3, the error is computed with regards to the final value obtained for each method. The two methods are not evaluated against the same final value because our method converges to a different value than the undisplaced mesh, by a few %. This small difference can be explained by the fact that the displaced mesh is always smooth, i.e. not pixelated, unlike the undisplaced mesh. This can be observed for example in Fig. 2. As shown in Fig. 3, this smoothness influences the results of permeability. The difference reduces, as expected, with increasing resolution of the CT scan.

For all rock samples, we can observe that the mesh convergence is not reached at the image resolution with the undisplaced method, as confirmed by Guibert et al. (2015). We only manage to fall under 2% of error at twice the initial image resolution, which is therefore selected as our reference for mesh convergence in this contribution (as denoted by the horizontal red line in the following figures). Note that Guibert et al. (2015) showed that even more accuracy can be achieved at four times the resolution of the initial image.

Using the displaced boundary method, we reach the mesh convergence for each sample, always earlier than with the undisplaced method. Interestingly though, the convergence is not reached for the same relative resolution. For the sandpack and the sandstone that have a similarly low spatial resolution, respectively 10.002 μm and 8.683 μm, the convergence is achieved around the initial image resolution. However, it is for the limestone which has a high spatial resolution of 3.00006 μm that our method performs the best. Mesh convergence is achieved at half of the image resolution. With regards to the other differences that we pointed out between the samples images, it seems that the resolution has the most influence on the performance of the displaced boundary method.

By comparing the displaced boundary method with the undisplaced method, we expose that there exists actually two different convergences when running a mesh convergence of permeability.

The displaced boundary method exposes two different influences on the mesh convergence of permeability for regular meshing. The first one is the convergence of the geometry of the pore–grain boundary. Indeed with a regular cartesian mesh, a matching geometry of the interface is only achieved at image resolution or one of its multiples. This could explain why Guibert et al. (2015) could not obtain a mesh

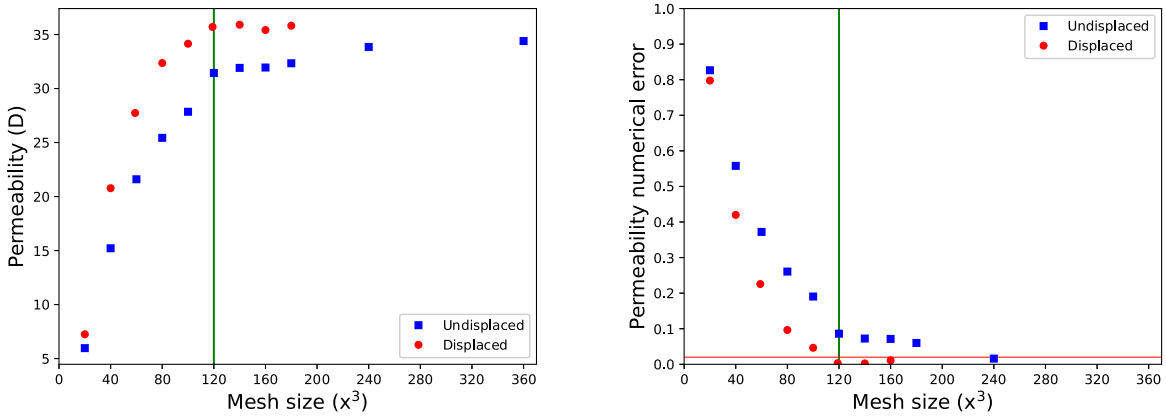

Fig. 6. Mesh convergence of the permeability of a sample of the LV60 A sandpack of size $(1.2\ \text{mm})^3$, with and without the displaced boundary method. The resolution of the original scan is 120^3 voxels. (a) shows absolute permeability computation and (b) the evolution of the permeability error compared to the final value.

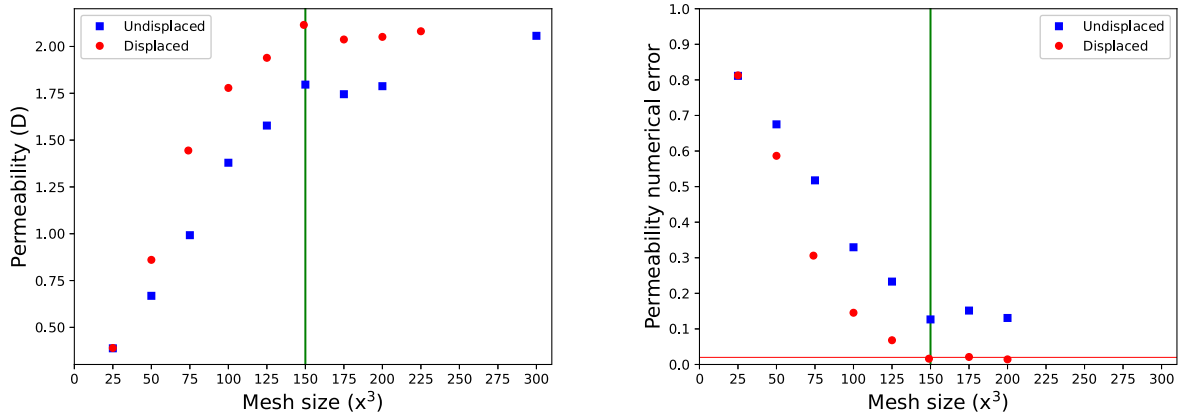

Fig. 7. Mesh convergence of the permeability of a sample of the S1 sandstone of size $(1.3\ \text{mm})^3$, with and without the displaced boundary method. The size of the original scan is 150^3 voxels. (a) shows absolute permeability computation and (b) the evolution of the permeability error compared to the final value.

convergence below the image resolution, because the geometry would always be approximated under this resolution. The advantage of using our method is to be able to have a good approximation of the interface very early. The second is the numerical mesh convergence itself. This one is achieved independently of the image resolution at a specific absolute value of mesh size h. High-resolution images seems to be the most interesting application of our method because, in that case, the numerical mesh convergence is reached much earlier than the convergence of the geometry. Since our method is not affected by the convergence of the geometry, we therefore obtain a global mesh convergence much earlier than with the undisplaced method, as shown for the limestone sample in Fig. 8.

To emphasise this last point, we run a mesh convergence of the same limestone sample but where the resolution was artificially lowered three times. The mesh convergence is plotted in Fig. 9. We note that the permeability with both methods converges approximately towards 5.5 Darcy, which differs from the value obtained with the high resolution CTscan in Fig. 8, around 7 Darcy. This can be explained by the bad approximation of the structure when using the low-resolution image. The permeability now converges only at image resolution with the displaced method, instead of earlier on the high resolution CTscan, which proves the better efficiency of the method for images that have a high resolution compared to the grain size.

4. Application to high-resolution CT scan

After demonstrating the efficiency of the displaced boundary method for permeability computation on rocks' μCT scan in the previous section, we apply it in the case where it is the most advantageous, for a high-resolution CT scan. We select again the Ketton carbonate on which our method has shown an impactful improvement on the cost of permeability computation (Fig. 8). However in this section, we select a larger sample, of 500^3 voxels in size, visualised in Fig. 10a. Since mesh convergence with the undisplaced method can only be reached at around two times the resolution of the original image, permeability should be computed on a sample of at least 1000^3 voxels. Since our system solves for the pressure and the velocity variables in each direction, this corresponds to solving for 4×10^9 Degrees Of Freedom (DOF). Running a flow simulation for such size requires obviously to be run on a supercomputer on which enormous memory allocation is needed. Yet we show in this section that the permeability of such a large sample can be retrieved easily with the displaced boundary method. In comparison, we also show how much error the undisplaced method still has at this point.

The mesh convergence of the two methods is plotted in Fig. 11, in absolute values and with the relative error. Contrary to the previous benchmarking section, we simulate a real application of the method. Therefore the convergence is assessed at each increment of size by evaluating the relative error compared to the previous size selected, unlike the previous section where the absolute numerical error is computed. Convergence is deemed reached under 2% error, as previously mentioned. It is achieved with the displaced boundary method at less than half the image resolution, similarly to Fig. 8. The improvement can be seen two ways. At the converged size of 200^3 voxels, it corresponds to a gain of 5% accuracy compared to the undisplaced method. On the other hand, if we expect the mesh convergence of this sample would normally be reached at 1000^3 voxels with the undisplaced method, using the displaced boundary method corresponds to reduces

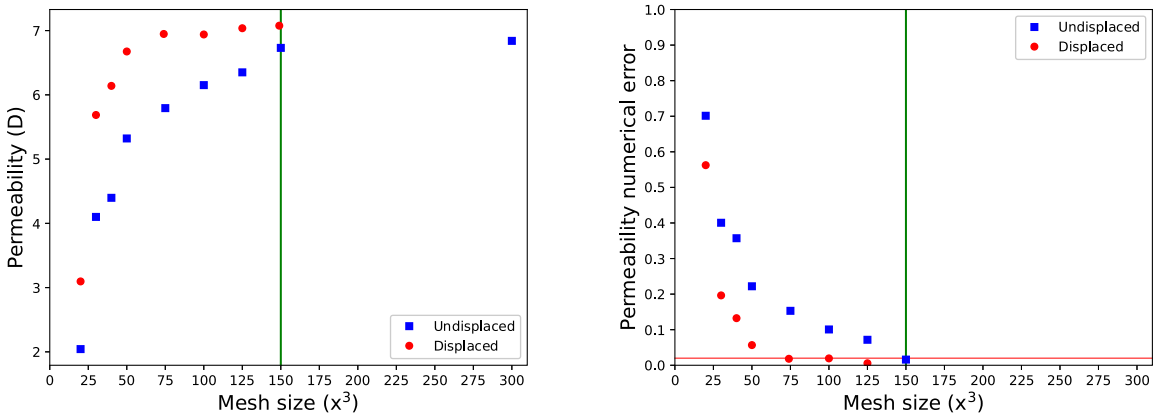

Fig. 8. Mesh convergence of the permeability of a sample of the Ketton carbonate of size $(0.45\ \text{mm})^3$, with and without the displaced boundary method. The size of the original scan is 150^3 voxels. (a) shows absolute permeability computation and (b) the evolution of the permeability error compared to the final value.

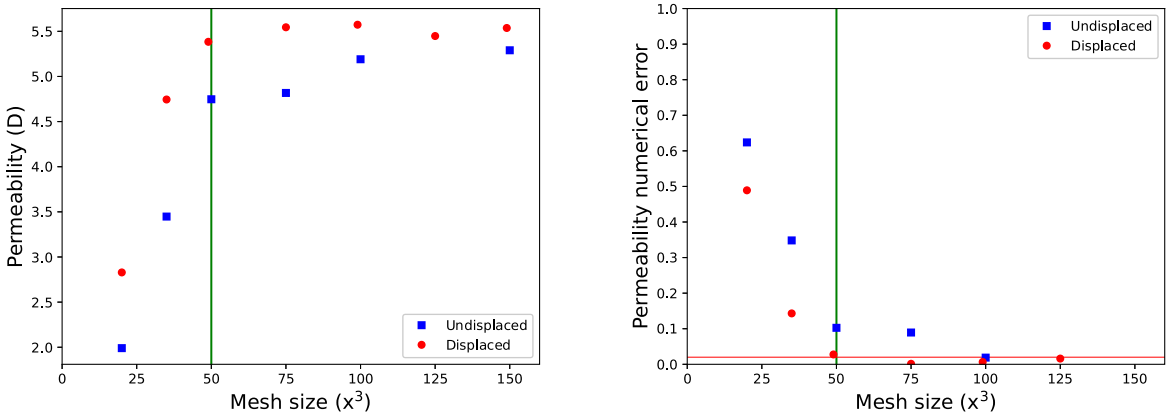

Fig. 9. Mesh convergence of the permeability of a sample of the Ketton carbonate of size $(0.45\ \text{mm})^3$, with and without the displaced boundary method. The size of the original scan is 50^3 voxels, three times coarsened from Fig. 5c. (a) shows absolute permeability computation and (b) the evolution of the permeability error compared to the final value.

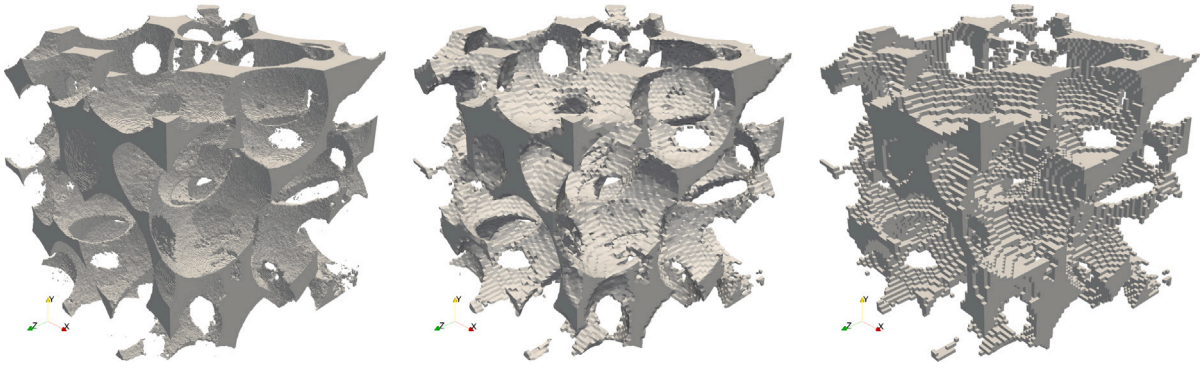

Fig. 10. Visualisation of meshed pore space of the Ketton sample of size $(1.5\ \text{mm})^3$. (a) is the original scan composed of 500^3 voxels ; (b) is meshed with 75^3 elements with the boundary displaced to fit (a) ; (c) is meshed undisplaced with 75^3 elements.

the computational size by $1000^3/200^3 = 125$, which is a consequent factor.

5. Conclusions

In this contribution tackling the common problem of computational cost of Digital Rock Physics, we have presented a method to improve the mesh convergence of permeability computations on μCT scan. We have managed to do so by approximating the pore–grain geometry of the digital microstructure more accurately than regular cartesian meshing techniques. The unfitted boundary method used is implemented in the MOOSE simulation platform. The simulations are performed for an equivalent mesh, in which the nodes of the cartesian mesh close to the boundary are displaced to the closest point on the exact interface. The method has been benchmarked on the semi-analytical solution of a regular sphere packing (Section 2.3), shown to improve mesh

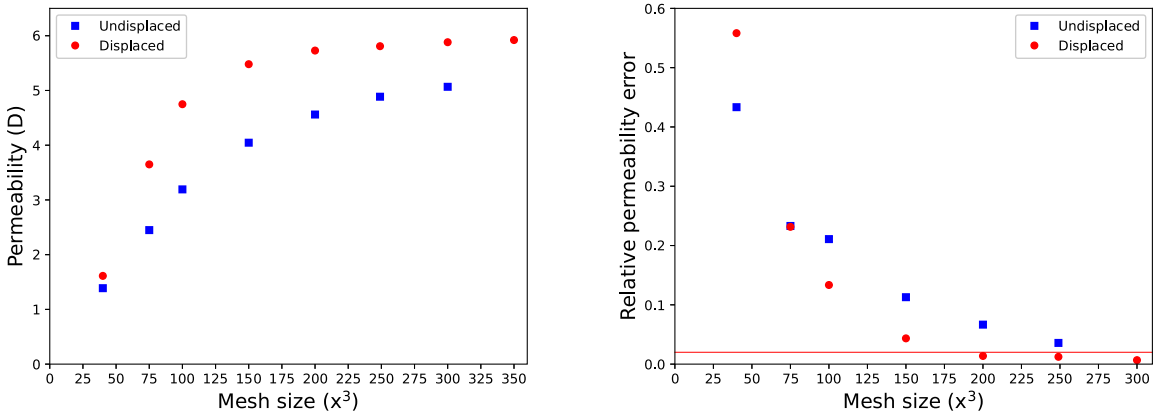

Fig. 11. Mesh convergence of the permeability of a sample of the Ketton carbonate of size $(1.5\ \text{mm})^3$, with and without the displaced boundary method. The size of the original scan is 500^3 voxels. (a) shows absolute permeability computation and (b) the evolution of the permeability error compared to the consecutive value.

convergence of permeability on three different digital rock samples of a sandpack, a sandstone and a limestone (Section 3) and finally applied to a high-resolution CT scan of a limestone (Section 4).

This numerical coarsening method allows to reach accurate values for the permeability for coarse meshes by obtaining a geometrically accurate pore–grain interface position and hence can save significantly the computation time required for flow simulation performed on digital rock microstructures. In order to obtain global mesh convergence of the permeability, we only need to satisfy the absolute numerical mesh convergence. For this reason, our method is expected to perform better for CT scans that have a high resolution compared to the rock's grain size, where the numerical mesh convergence is reached even for meshes coarser than the image resolution. Still, the displaced boundary method has been applied in this contribution to μCT images of digital rocks obtained after relatively coarse voxelised segmentation obtained by a global thresholding method and achieved mesh convergence always earlier than the undisplaced method. However, the rapid development conventional X ray and synchrotron based CT scans (Tengattini et al., 2021) and image enhancement methods (Sheppard et al., 2004) enable to produce high quality, high-resolution images that are optimised for further segmentation and grey scale analysis of large samples. On top of these developments, more elaborate segmentation methods like level set methods (Caselles et al., 1997) or a watershed finding combined with a fast marching algorithm (Sheppard et al., 2004) allow to preserve smaller details of the microstructure after segmentation and leads therefore to a more resolved pore–grain interface. This unfitted boundary method would prove particularly useful by taking profit of the very high-resolution pore–grain boundary resulting from more complex segmentation processes.

Finally, this method has only been applied here in the case of a static interface. However, multi-physical processes like mechanical deformations of the solid matrix (Lesueur et al., 2017) or dissolution–precipitation mechanisms (Lesueur et al., 2020; Rattez et al., 2021; Guével et al., 2020) induce a displacement of the interface, which cannot remain static during a simulation. The unfitted boundary method applied to flow coupled to these processes would allow to track accurately and in a continuous way the interface without at the same time requiring a very fine mesh.

Computer code availability

All results presented in this study were obtained with the open-source REDBACK simulator (Poulet et al., 2017) (http://github.com/pou036/redback), a MOOSE module (Permann et al., 2020) under GNU Lesser General Public License.

CRediT authorship contribution statement

Martin Lesueur: Conceptualization, Methodology, Software, Investigation, Writing. **Hadrien Rattez:** Conceptualization, Methodology, Writing. **Oriol Colomés:** Conceptualization, Methodology, Writing.

Declaration of competing interest

The authors declare that they have no known competing financial interests or personal relationships that could have appeared to influence the work reported in this paper.

References

Ahmed, U., Crary, S.F., Coates, G.R., 1991. Permeability estimation. The various sources and their interrelationships. J. Pet. Technol. 43 (5), 578–587. http://dx.doi.org/10.2118/19604-PA.

Andrä, H., Combaret, N., Dvorkin, J., Glatt, E., Han, J., Kabel, M., Keehm, Y., Krzikalla, F., Lee, M., Madonna, C., Marsh, M., Mukerji, T., Saenger, E.H., Sain, R., Saxena, N., Ricker, S., Wiegmann, A., Zhan, X., 2013. Digital rock physics benchmarks—Part I: Imaging and segmentation. Comput. Geosci. 50, 25–32. http://dx.doi.org/10.1016/j.cageo.2012.09.005.

Arns, C.H., Bauget, F., Limaye, A., Sakellariou, A., Senden, T., Sheppard, A., Sok, R.M., Pinczewski, V., Bakke, S., Berge, L.I., Oren, P.E., Knackstedt, M.A., 2005. Pore scale characterization of carbonates using X-Ray microtomography. SPE J. 10 (04), 475–484. http://dx.doi.org/10.2118/90368-pa.

Arns, C.H., Knackstedt, M.A., Pinczewski, W.V., Garboczi, E.J., 2002. Computation of linear elastic properties from microtomographic images: Methodology and agreement between theory and experiment. Geophysics 67 (5), 1396–1405. http://dx.doi.org/10.1190/1.1512785.

Arns, C.H., Knackstedt, M.A., Pinczewski, W.V., Martys, N.S., 2004. Virtual permeametry on microtomographic images. J. Pet. Sci. Eng. 45 (1–2), 41–46. http://dx.doi.org/10.1016/j.petrol.2004.05.001.

Balay, S., Abhyankar, S., Adams, M.F., Brown, J., Brune, P., Buschelman, K., Dalcin, L., Eijkhout, V., Gropp, W.D., Kaushik, D., Knepley, M.G., McInnes, L.C., Rupp, K., Smith, B.F., Zampini, S., Zhang, H., 2016. PETSc Users Manual. Technical Report ANL-95/11 - Revision 3.7, Argonne National Laboratory.

Beard, D.C., Weyl, P.K., 1973. Influence of texture on porosity and permeability of unconsolidated sand. AAPG Bull. 57, http://dx.doi.org/10.1306/819a4272-16c5-11d7-8645000102c1865d.

Bertrand, F., Cerfontaine, B., Collin, F., 2017. A fully coupled hydro-mechanical model for the modeling of coalbed methane recovery. J. Nat. Gas Sci. Eng. 46, 307–325. http://dx.doi.org/10.1016/j.jngse.2017.07.029.

Bjorlykke, K., 2010. Petroleum geoscience: From sedimentary enviroments to rock physics. p. 508. http://dx.doi.org/10.1007/978-3-642-02332-3, arXiv:arXiv:1011.1669v3.

Blunt, M.J., Bijeljic, B., Dong, H., Gharbi, O., Iglauer, S., Mostaghimi, P., Paluszny, A., Pentland, C., 2013. Pore-scale imaging and modelling. Adv. Water Resour. 51, 197–216. http://dx.doi.org/10.1016/j.advwatres.2012.03.003.

Borujeni, A.T., Lane, N., Thompson, K., Tyagi, M., 2013. Effects of image resolution and numerical resolution on computed permeability of consolidated packing using LB and FEM pore-scale simulations. Comput. & Fluids 88, 753–763. http://dx.doi.org/10.1016/j.compfluid.2013.05.019.

Burghardt, A.J., Kazakia, G.J., Majumdar, S., 2007. A local adaptive threshold strategy for high resolution peripheral quantitative computed tomography of trabecular bone. Ann. Biomed. Eng. 35 (10), 1678–1686. http://dx.doi.org/10.1007/s10439-007-9344-4.

Burman, E., Claus, S., Hansbo, P., Larson, M.G., Massing, A., 2015. Cutfem: discretizing geometry and partial differential equations. Internat. J. Numer. Methods Engrg. 104 (7), 472–501.

Burman, E., Fernández, M.A., 2011. Analysis of the PSPG method for the transient Stokes' problem. Comput. Methods Appl. Mech. Engrg. 200 (41–44), 2882–2890.

Caselles, V., Kimmel, R., Sapiro, G., 1997. Geodesic active contours. Int. J. Comput. Vis. 22 (1), 61–79. http://dx.doi.org/10.1023/A:1007979827043.

Cnudde, V., Boone, M., 2013. High-resolution X-ray computed tomography in geosciences: A review of the current technology and applications. Earth-Sci. Rev. 123, 1–17. http://dx.doi.org/10.1016/j.earscirev.2013.04.003.

Codina, R., Badia, S., Baiges, J., Principe, J., 2018. Variational multiscale methods in computational fluid dynamics. In: Encyclopedia of Computational Mechanics Second Edition. Wiley Online Library, pp. 1–28.

Codina, R., Blasco, J., 2000. Analysis of a pressure-stabilized finite element approximation of the stationary Navier-Stokes equations. Numer. Math. 87 (1), 59–81.

Colomés, O., Badia, S., Codina, R., Principe, J., 2015. Assessment of variational multiscale models for the large eddy simulation of turbulent incompressible flows. Comput. Methods Appl. Mech. Engrg. 285, 32–63.

Cox, M.R., Budhu, M., 2008. A practical approach to grain shape quantification. Eng. Geol. 96 (1–2), 1–16. http://dx.doi.org/10.1016/j.enggeo.2007.05.005.

Darcy, H.P.G., 1856. Détermination des lois d'écoulement de l'eau à travers le sable. In: Les Fontaines Publiques de la Ville de Dijon. V. Dalamont, pp. 590–594.

Donea, J., Giuliani, S., Halleux, J.-P., 1982. An arbitrary Lagrangian-Eulerian finite element method for transient dynamic fluid-structure interactions. Comput. Methods Appl. Mech. Engrg. 33 (1–3), 689–723.

Dvorkin, J., Armbruster, M., Baldwin, C., Fang, Q., Derzhi, N., Gomez, C., Nur, B., Nur, A., 2008. The future of rock physics: computational methods vs. lab testing. First Break 26 (9), http://dx.doi.org/10.3997/1365-2397.26.1292.28600.

Elman, H., Howle, V.E., Shadid, J., Shuttleworth, R., Tuminaro, R., 2008. A taxonomy and comparison of parallel block multi-level preconditioners for the incompressible Navier–Stokes equations. J. Comput. Phys. 227 (3), 1790–1808. http://dx.doi.org/10.1016/j.jcp.2007.09.026.

Gerke, K.M., Vasilyev, R.V., Khirevich, S., Collins, D., Karsanina, M.V., Sizonenko, T.O., Korost, D.V., Lamontagne, S., Mallants, D., 2018. Finite-difference method Stokes solver (FDMSS) for 3D pore geometries: Software development, validation and case studies. Comput. Geosci. 114, 41–58. http://dx.doi.org/10.1016/j.cageo.2018.01.005.

Ghabezloo, S., Sulem, J., Saint-Marc, J., 2009. Evaluation of a permeability–porosity relationship in a low-permeability creeping material using a single transient test. Int. J. Rock Mech. Min. Sci. 46 (4), 761–768. http://dx.doi.org/10.1016/j.ijrmms.2008.10.003.

Godel, B., 2013. High-resolution X-Ray computed tomography and its application to ore deposits: From data acquisition to quantitative three-dimensional measurements with case studies from Ni-cu-PGE deposits. Econ. Geol. 108 (8), 2005–2019. http://dx.doi.org/10.2113/econgeo.108.8.2005.

Guével, A., Rattez, H., Veveakis, M., 2020. Viscous phase-field modeling for chemo-mechanical microstructural evolution: application to geomaterials and pressure solution. Int. J. Solids Struct. 207, 230–249. http://dx.doi.org/10.1016/j.ijsolstr.2020.09.026.

Guibert, R., Nazarova, M., Horgue, P., Hamon, G., Creux, P., Debenest, G., 2015. Computational permeability determination from pore-scale imaging: Sample size, mesh and method sensitivities. Transp. Porous Media 107 (3), 641–656. http://dx.doi.org/10.1007/s11242-015-0458-0.

Henson, V.E., Yang, U.M., 2002. BoomerAMG: A parallel algebraic multigrid solver and preconditioner. Appl. Numer. Math. 41 (1), 155–177. http://dx.doi.org/10.1016/s0168-9274(01)00115-5.

Hughes, T.J., Feijóo, G.R., Mazzei, L., Quincy, J.-B., 1998. The variational multiscale method—a paradigm for computational mechanics. Comput. Methods Appl. Mech. Engrg. 166 (1–2), 3–24.

Hughes, T.J., Franca, L.P., Balestra, M., 1986. A new finite element formulation for computational fluid dynamics: V. Circumventing the Babuška-Brezzi condition: A stable Petrov-Galerkin formulation of the Stokes problem accommodating equal-order interpolations. Comput. Methods Appl. Mech. Engrg. 59 (1), 85–99.

Iassonov, P., Gebrenegus, T., Tuller, M., 2009. Segmentation of X-ray computed tomography images of porous materials: A crucial step for characterization and quantitative analysis of pore structures. Water Resour. Res. 45 (9), http://dx.doi.org/10.1029/2009wr008087.

Imperial College Consortium On Pore-Scale Modelling, 2014a. LV60A sandpack. http://dx.doi.org/10.6084/m9.figshare.1153795.

Imperial College Consortium On Pore-Scale Modelling, 2014b. S1 sandstone. http://dx.doi.org/10.6084/m9.figshare.1189274.v1.

Jacobson, A., Panozzo, D., et al., 2018. libigl: A simple C++ geometry processing library. https://libigl.github.io/.

Larson, R.E., Higdon, J.J.L., 1989. A periodic grain consolidation model of porous media. Phys. Fluids A 1 (1), 38–46. http://dx.doi.org/10.1063/1.857545.

Lesueur, M., Casadiego, M.C., Veveakis, M., Poulet, T., 2017. Modelling fluid-microstructure interaction on elasto-visco-plastic digital rocks. Geomech. Energy Environ. 12, 1–13. http://dx.doi.org/10.1016/j.gete.2017.08.001.

Lesueur, M., Poulet, T., Veveakis, M., 2020. Three-scale multiphysics finite element framework (FE3) modelling fault reactivation. Comput. Methods Appl. Mech. Engrg. 365, 112988. http://dx.doi.org/10.1016/j.cma.2020.112988.

Liu, J., Pereira, G.G., Regenauer-Lieb, K., 2014. From characterisation of pore-structures to simulations of pore-scale fluid flow and the upscaling of permeability using microtomography: A case study of heterogeneous carbonates. J. Geochem. Explor. 144, 84–96. http://dx.doi.org/10.1016/j.gexplo.2014.01.021.

Lorensen, W.E., Cline, H.E., 1987. Marching cubes: A high resolution 3D surface construction algorithm. In: Proceedings of the 14th Annual Conference on Computer Graphics and Interactive Techniques, SIGGRAPH 1987, Vol. 21. pp. 163–169. http://dx.doi.org/10.1145/37401.37422.

Manwart, C., Aaltosalmi, U., Koponen, A., Hilfer, R., Timonen, J., 2002. Lattice-Boltzmann and finite-difference simulations for the permeability for three-dimensional porous media. Phys. Rev. E 66 (1), http://dx.doi.org/10.1103/physreve.66.016702.

Mees, F., Swennen, R., Geet, M.V., Jacobs, P., 2003. Applications of X-ray computed tomography in the geosciences. Geol. Soc. Lond. Spec. Publ. 215 (1), 1–6. http://dx.doi.org/10.1144/gsl.sp.2003.215.01.01.

Mittal, R., Iaccarino, G., 2005. Immersed boundary methods. Annu. Rev. Fluid Mech. 37, 239–261.

Mostaghimi, P., Blunt, M.J., Bijeljic, B., 2012. Computations of absolute permeability on micro-CT images. Math. Geosci. 45 (1), 103–125. http://dx.doi.org/10.1007/s11004-012-9431-4.

Narváez, A., Yazdchi, K., Luding, S., Harting, J., 2013. From creeping to inertial flow in porous media: a lattice Boltzmann–finite element study. J. Stat. Mech. Theory Exp. 2013 (02), 2–38. http://dx.doi.org/10.1088/1742-5468/2013/02/p02038.

Permann, C.J., Gaston, D.R., Andrš, D., Carlsen, R.W., Kong, F., Lindsay, A.D., Miller, J.M., Peterson, J.W., Slaughter, A.E., Stogner, R.H., Martineau, R.C., 2020. MOOSE: Enabling massively parallel multiphysics simulation. SoftwareX 11, 100430. http://dx.doi.org/10.1016/j.softx.2020.100430, URL: http://www.sciencedirect.com/science/article/pii/S2352711019302973.

Peterson, J.W., Lindsay, A.D., Kong, F., 2018. Overview of the incompressible Navier–Stokes simulation capabilities in the MOOSE framework. Adv. Eng. Softw. 119, 68–92. http://dx.doi.org/10.1016/j.advengsoft.2018.02.004.

Petrasch, J., Meier, F., Friess, H., Steinfeld, A., 2008. Tomography based determination of permeability, Dupuit–Forchheimer coefficient, and interfacial heat transfer coefficient in reticulate porous ceramics. Int. J. Heat Fluid Flow 29 (1), 315–326. http://dx.doi.org/10.1016/j.ijheatfluidflow.2007.09.001.

Poulet, T., Paesold, M., Veveakis, M., 2017. Multi-physics modelling of fault mechanics using REDBACK: A parallel open-source simulator for tightly coupled problems. Rock Mech. Rock Eng. 50 (3), 733–749. http://dx.doi.org/10.1007/s00603-016-0927-y.

Rangarajan, R., Lew, A.J., 2014. Universal meshes: A method for triangulating planar curved domains immersed in nonconforming meshes. Internat. J. Numer. Methods Engrg. 98 (4), 236–264. http://dx.doi.org/10.1002/nme.4624.

Rattez, H., Disidoro, F., Sulem, J., Veveakis, M., 2021. Influence of dissolution on long-term frictional properties of carbonate fault gouge. Geomech. Energy Environ. 26, 100234. http://dx.doi.org/10.1016/j.gete.2021.100234.

Salvo, L., Cloetens, P., Maire, E., Zabler, S., Blandin, J.J., Buffière, J.Y., Ludwig, W., Boller, E., Bellet, D., Josserond, C., 2003. X-ray micro-tomography an attractive characterisation technique in materials science. Nucl. Instrum. Methods Phys. Res. Sect. B 200, 273–286. http://dx.doi.org/10.1016/S0168-583X(02)01689-0.

Sangani, A., Acrivos, A., 1982. Slow flow through a periodic array of spheres. Int. J. Multiph. Flow. 8 (4), 343–360. http://dx.doi.org/10.1016/0301-9322(82)90047-7.

Sarker, M., Siddiqui, S., 2009. Advances in micro-CT based evaluation of reservoir rocks. In: SPE Saudi Arabia Section Technical Symposium. Society of Petroleum Engineers, http://dx.doi.org/10.2118/126039-ms.

Shah, S., Gray, F., Crawshaw, J., Boek, E., 2016. Micro-computed tomography pore-scale study of flow in porous media: Effect of voxel resolution. Adv. Water Resour. 95, 276–287. http://dx.doi.org/10.1016/j.advwatres.2015.07.012.

Sheppard, A.P., Sok, R.M., Averdunk, H., 2004. Techniques for image enhancement and segmentation of tomographic images of porous materials. Physica A 339 (1–2), 145–151. http://dx.doi.org/10.1016/j.physa.2004.03.057.

Song, R., Wang, Y., Liu, J., Cui, M., Lei, Y., 2019. Comparative analysis on pore-scale permeability prediction on micro-CT images of rock using numerical and empirical approaches. Energy Sci. Eng. 7 (6), 2842–2854. http://dx.doi.org/10.1002/ese3.465.

Soulaine, C., Gjetvaj, F., Garing, C., Roman, S., Russian, A., Gouze, P., Tchelepi, H.A., 2016. The impact of sub-resolution porosity of X-ray microtomography images on the permeability. Transp. Porous Media 113 (1), 227–243. http://dx.doi.org/10.1007/s11242-016-0690-2.

Tengattini, A., Lenoir, N., Andò, E., Viggiani, G., 2021. Neutron imaging for geomechanics: A review. Geomech. Energy Environ. 27, 100206. http://dx.doi.org/10.1016/j.gete.2020.100206.

Tezduyar, T., Sathe, S., 2003. Stabilization parameters in SUPG and PSPG formulations. J. Comput. Appl. Mech. 4 (1), 71–88.

Torskaya, T., Shabro, V., Torres-Verdín, C., Salazar-Tio, R., Revil, A., 2013. Grain shape effects on permeability, formation factor, and capillary pressure from pore-scale modeling. Transp. Porous Media 102 (1), 71–90. http://dx.doi.org/10.1007/s11242-013-0262-7.

Tuan, H.S., Hutmacher, D.W., 2005. Application of micro CT and computation modeling in bone tissue engineering. Comput. Aided Des. 37 (11), 1151–1161. http://dx.doi.org/10.1016/j.cad.2005.02.006.

Wang, Y.D., Armstrong, R.T., Mostaghimi, P., 2019a. Enhancing resolution of digital rock images with super resolution convolutional neural networks. J. Pet. Sci. Eng. 182, 106261. http://dx.doi.org/10.1016/j.petrol.2019.106261.

Wang, Y.D., Chung, T., Armstrong, R.T., McClure, J.E., Mostaghimi, P., 2019b. Computations of permeability of large rock images by dual grid domain decomposition. Adv. Water Resour. 126, 1–14. http://dx.doi.org/10.1016/j.advwatres.2019.02.002.

Wang, J., Fleischmann, D., 2018. Improving spatial resolution at CT: Development, benefits, and pitfalls. Radiology 289 (1), 261–262. http://dx.doi.org/10.1148/radiol.2018181156.

Whitaker, S., 1986. Flow in porous media I: A theoretical derivation of Darcy's law. Transp. Porous Media 1 (1), 3–25. http://dx.doi.org/10.1007/bf01036523.

Yan, Z., Matuszewski, B.J., Shark, L.K., Moore, C.J., 2008. Medical image segmentation using new hybrid level-set method. In: Proceedings - 5th International Conference BioMedical Visualization, Information Visualization in Medical and Biomedical Informatics, MediVis 2008. pp. 71–76. http://dx.doi.org/10.1109/MediVis.2008.12.

Yang, L., Yang, J., Boek, E., Sakai, M., Pain, C., 2019. Image-based simulations of absolute permeability with massively parallel pseudo-compressible stabilised finite element solver. Comput. Geosci. 23 (5), 881–893. http://dx.doi.org/10.1007/s10596-019-09837-4.

Zakirov, T., Galeev, A., 2019. Absolute permeability calculations in micro-computed tomography models of sandstones by Navier-Stokes and lattice Boltzmann equations. Int. J. Heat Mass Transfer 129, 415–426. http://dx.doi.org/10.1016/j.ijheatmasstransfer.2018.09.119.

Zick, A.A., Homsy, G.M., 1982. Stokes flow through periodic arrays of spheres. J. Fluid Mech. 115, 13. http://dx.doi.org/10.1017/s0022112082000627.